Chemical Geology 346 (2013) 3–13

Contents lists available at SciVerse ScienceDirect

Chemical Geology

journal homepage: www.elsevier.com/locate/chemgeo

The influence of composition on the local structure around yttrium in quenched silicate melts — Insights from EXAFS

S. Simon [a,*], M. Wilke [a], R. Chernikov [b], S. Klemme [c], L. Hennet [d]

[a] Deutsches GeoForschungsZentrum GFZ, Telegrafenberg, 14473 Potsdam, Germany
[b] Deutsches Elektronen-Synchrotron, DESY, Notkestraße 85, 22607 Hamburg, Germany
[c] Institut für Mineralogie, Westfälische Wilhelms-Universität, Corrensstr. 24, 48149 Münster, Germany
[d] CNRS-CEMHTI, 45071 Orleans CEDEX 2, France

ARTICLE INFO

Article history:
Accepted 10 September 2012
Available online 17 September 2012

Keywords:
Yttrium
Local structure
Quenched silicate melts
EXAFS
Gamma-like distribution function

ABSTRACT

The structural environment around Y in silicate and aluminosilicate glasses containing 5000 ppm Y was investigated as a function of melt composition and polymerization using Extended X-ray Absorption Fine Structure (EXAFS) spectroscopy. The used glass compositions were taken from Prowatke and Klemme (2005) varying in the aluminum saturation index (ASI, molar ratio of $Al_2O_3/(Na_2O+K_2O+CaO)$) from 0.115 to 0.768. Furthermore, a set of glass compositions from the system $CaO–Al_2O_3–SiO_2$ (CAS) was used, for which structural data from computer simulations are available (Haigis et al., 2013–this issue). Structural parameters of the Y–O pair correlation of the first coordination shell were determined from the EXAFS based on a gamma-like distribution function that accounts for the large static disorder and non-Gaussian pair distributions. The analysis shows an increase in the coordination number from 6 to 8, along with an increase of the average Y–O distance by 0.13 Å for the composition of Prowatke and Klemme (2005). For the CAS-composition an increase of the coordination number from 6 to 7, along with an increase of the average Y–O distance by 0.06 Å is obtained. The change of these parameters is associated with a considerable increase in the asymmetry and width of the Y–O pair distribution. Due to its size and charge, 6-fold coordinated Y will preferentially bond to non-bridging oxygens of the polymeric melt network to form a stable configuration, as is the case for the less polymerized melts with low ASI. In highly polymerized melts with ASI values close to one, 6-fold coordination of Y is not possible because almost only bridging oxygens are available. Consequently, over-bonding of bridging oxygens around Y is counterbalanced by an increase of coordination number and Y–O distance to satisfy local charge balance requirements.

1. Introduction

Trace elements are important indicators for processes that lead to the formation of magmatic and metamorphic rocks on Earth, Moon and the terrestrial planets. In order to interpret observed trace element variations in these rocks, one needs to understand the physical and chemical parameters which govern the partitioning of trace elements between crystals and melts. It is well known that temperature, pressure and oxygen fugacity (in case of elements that change their oxidation state under geologically relevant conditions) are important parameters controlling trace element fractionation (see Green (1994) for a review). In terms of chemical composition, both crystal and melt composition may influence partitioning. The effect of the crystal composition was first recognized by Goldschmidt (1937). He found that the size and charge of the trace element play an important role for their incorporation. Onuma et al. (1968) recognized a parabolic relationship between the partition coefficient ($D_{crystal/melt}$) of trace elements and their ionic radius. They showed that the maximum of the parabola coincides with the ionic radius of Mg, the major cation on the octahedral lattice site in bronzite pyroxene. Eventually, this led to the model developed by Blundy and Wood (1994), which linked the parabolic correlation between $D_{crystal/melt}$ and ionic radius with the ideal size of the lattice site — the so-called "lattice strain model" (Brice, 1975). To improve this model, Wood and Blundy (2001) included the charge of the substituting ion. This new model assumes that if a cation is replaced by an ion with approximately the same radius the $D_{crystal/melt}$ depends only on the charge of that ion.

However, while crystal chemical effects on partitioning are well understood (e.g., Wood and Blundy, 1997; 2001), the effect of melt composition on trace element partitioning is still not clear. Several early experimental studies indicate also considerable dependence of element partitioning on melt composition (Hart and Davis, 1978; Irving, 1978; van Westrenen et al., 2001; Toplis and Corgne, 2002). The strongest effects are observed with varying SiO_2 and MgO content of the melt but other parameters such as Mg/Fe ratio, alkali content, alkalis/Al ratio, P-content of the melt play an important role as

* Corresponding author at: Telegrafenberg, 14473 Potsdam, Germany. Tel.: +49 331 288 1894; fax: +331 288 1402.
E-mail address: ssimon@gfz-potsdam.de (S. Simon).

0009-2541/$ – see front matter © 2012 Elsevier B.V. All rights reserved.
http://dx.doi.org/10.1016/j.chemgeo.2012.09.017

controlling factors for $D_{crystal/melt}$. There is also evidence that H_2O, Cl_2, CO_2 and other volatile components may affect $D_{crystal/melt}$ (e.g. Carroll and Webster, 1994). The influence of melt composition on the partition coefficients was usually assigned to differences in the melt structure, and thus seemed to imply changes in the structural environment of the trace element. However, in many of these studies mentioned above it is difficult to disentangle the melt effect from other parameters. To address these matters, Prowatke and Klemme (2005) specifically investigated the influence of the melt composition on the partitioning of a suite of trace elements between titanite and different melt compositions. They systematically varied the aluminum saturation index (ASI; molar ratio of $Al_2O_3/(Na_2O+K_2O+CaO)$) of the melt, while ensuring that pressure, temperature, and the crystal composition remained constant over the entire compositional space explored. For their suite of trace elements, Prowatke and Klemme (2005) obtained a correlation between $D_{crystal/melt}$ and the ASI of the melt composition. They report that the $D_{crystal/melt}$ of the rare earth elements (REE) and of Th, Nb, and Ta are strongly affected by the melt composition. For the REE, the $D_{crystal/melt}$ varied over two (e.g. La, Yb) or three orders of magnitude (e.g. Gd, Sm). For Nb and Ta, $D_{crystal/melt}$ varied over one order of magnitude and for Th, the $D_{crystal/melt}$ varied over two orders of magnitude (Prowatke and Klemme, 2005). In contrast, they found that the partition coefficients of e.g., Cs, Sr, Zr, and Hf are not significantly affected by melt composition.

Another approach to investigate the effect of melt composition on trace element partitioning is to study immiscible melts. This was done in the system K_2O–Al_2O_3–FeO–SiO_2 (Watson, 1976; Ryerson and Hess, 1978; Schmidt et al., 2006). Results from these studies showed that cations with a high charge density (i.e., charge/cation radius) like transition metals, REE, and high field strength elements (HFSE) prefer to enter the more basic melt whereas low charge density cations such as Cs preferentially partition into the immiscible acidic melt. Cations with intermediate charge density like Sr and Ba showed only little fractionation between the two immiscible melts.

The aforementioned experimental studies clearly show that melt composition is an important factor in element partitioning, and this clearly needs to be considered for predictive models of trace element partitioning. However, in order to better understand the influence of melt composition on trace element partitioning, one needs to understand the structural incorporation of trace elements in melts. It is well known that the structure of the melt is strongly dependent on melt composition and which in turn defines the coordination sites that host the trace elements. Thus, it is important to understand the relation between melt composition, melt structure and finally the local structure around trace elements, i.e. the coordination of the trace elements, in the melt.

Structural models of silicate melts are based on a polymeric network of corner-sharing SiO_4^{4-} tetrahedra. The degree of polymerization strongly depends on the melt composition (e.g. Mysen and Richet, 2005) and the ratio of network-modifying cations (e.g. Na, K, Ca, and Mg) to network-forming cations (Si, Al) defines the degree of polymerization. A parameter called NBO/T is often used to describe the degree of polymerization of silicate melts. This is a simple and elegant way to approximate melt structure, linking the ratio of non-bridging oxygens (NBO) to tetrahedrally coordinated cations (i.e. Si, Al) (Mysen et al., 1985; Mysen, 1990). The NBO/T is calculated by the equation $NBO/T = 2\,(NM - T^{3+})/T^{4+}$, where NM is the number of network modifying cations, T^{3+} number of tetrahedral cations that are charge-balanced by network modifiers (Al^{3+}, Fe^{3+}) and T^{4+} the number of remaining network forming cations (Si). For example, NBO/T = 0 describes a fully polymerized melt with four bridging oxygens around the tetrahedrally coordinated cations and NBO/T = 4 represents a completely depolymerized melt with four non-bridging oxygens. However, it should be noted that the NBO/T parameter is calculated from the chemical composition of the melt based on several simplifying assumptions. There are several ions for which the role in the melt structure is not sufficiently understood. Earlier recipes for calculation of NBO/T include for example Ti as network-forming cation (Mysen et al., 1985). However, Farges et al. (1996a) reported that the coordination of Ti is not unique and may vary depending on composition between 4-fold coordinated and 4 + 5-fold coordinated Ti. This is clear evidence for the fact that Ti does not act as normal network-forming cation. In aluminosilicate melts Al is predominantly 4-fold coordinated and acts as network-former. However, there is evidence that in peraluminous compositions small amounts of 5-fold and 6-fold coordinated Al are present (Risbud et al., 1987; Poe et al., 1992; Neuville et al., 2006). In strongly peraluminous compositions some 4-fold coordinated Al forms aluminum triclusters for charge compensation without metal cation (Stebbins et al., 2001; Kubicki and Toplis, 2002). Both examples evidence that the parameter NBO/T does not necessarily represent a useful approximation for the melt polymerization, especially for complex melt compositions.

Another approach to quantify the degree of polymerization is the ASI. It describes the molar ratio between Al and the network modifying cations (usually alkaline and earth alkaline elements). At a constant Si/Al ratio, an increase of the ASI number up to a value of one (metaluminous melts) would indicate an increase of the polymerization.

In order to derive structural information of minor and trace elements in melts or glasses a sensitive, possibly chemically selective, probe for the local structure of glasses and melts is needed. Extended X-ray Absorption Fine Structure (EXAFS) spectroscopy is a suitable method that provides insight into the local structure even at low concentrations. Ponader and Brown (1989) used this technique to investigate the coordination of REE (La, Gd, and Yb) in quenched melts of various simplified compositions. They showed that REE–O distance, the coordination number of the REE as well as the degree of disorder around the REE changes with increasing polymerization of the glass. For example, they found that the coordination of Gd changes from $^{[8]}$Gd to $^{[6]}$Gd along with a decrease in the average bond length from 2.43 Å to 2.30 Å. Ponader and Brown (1989) argued that these differences in the structural environment may explain differences in crystal–melt partitioning, in general. Farges et al. investigated various incompatible trace elements in quenched melts and also reported significant influence of the melt composition on the local structure around the trace element studied. For example, Th coordination changes from $^{[6]}$Th to $^{[8]}$Th, the average Th – O bond length increases from 2.32 ± 0.02 Å to 2.42 ± 0.02 Å with decreasing NBO/T of the melt/glass (Farges, 1991). Moreover, the Zr coordination number changes from $^{[6]}$Zr to $^{[8]}$Zr, the average Zr – O bond length increases from 2.07 ± 0.01 Å to 2.22 ± 0.01 Å with increasing polymerization of the melt (Farges et al., 1991). It should be noted that this constitutes the opposite trend when compared to the results for the REE by Ponader and Brown (1989).

Furthermore, there are several spectroscopic studies on REE in non-natural melt compositions, mainly related to technical applications. Peters and Houde-Walter (1997) investigated Er in quenched melts with compositions ranging from aluminosilicate to fluorosilicate and report a change of the coordination from $^{[6]}$Er to $^{[7]}$Er together with an increase of the average bond length across this compositional join. Mountjoy et al. (2001) studied various phosphate glasses with several REE (Nd, Eu, and Yb) as main components. They also found significant increase of bond length and a change of the coordination from $^{[6]}$REE to $^{[8]}$REE in melts ranging from meta- to ultraphosphate composition.

The aforementioned studies have provided valuable insights into the local structure of trace elements in silicate melts and were helpful to unravel the mechanism by which trace elements are incorporated in melts. However, no study has attempted to directly correlate the observed melt compositional effects in element partitioning with the differences in the local structure of the trace elements in the corresponding (quenched) melts.

The present study aims at addressing these matters by investigating the local structure of REE in quenched melts with exactly the same melt compositions used in the partitioning experiments of

Prowatke and Klemme (2005). This data set seems ideally suited because the variation of the partition coefficients can be completely assigned to differences in the melt composition and melt structure. We present data on Y serving as an analog for the heavy REE. The choice of Y enables us to collect EXAFS spectra at the K-edge at relatively low X-ray energies. In addition to the composition by Prowatke and Klemme, we studied three compositions from the system $CaO–Al_2O_3–SiO_2$, namely $CaSiO_3$, $Ca_3Al_2Si_3O_{12}$, and $CaAl_2Si_2O_8$ with NBO/T values of 2, 0.8 and 0. These compositions are related to a separate theoretical study on Y incorporation in silicate melts based on molecular dynamics (MD) simulation techniques (Haigis et al., 2013–this issue). From the MD simulations, information on the local structure of Y is obtained and used to estimate differences in free energy of Y between the compositions by thermodynamic integration in order to derive ab-initio constraints on the partitioning of Y. This data set is particularly suitable to test our analytical procedure applied to the EXAFS spectra by comparison to the trajectories and structural parameters derived from the simulations. Since analysis of EXAFS spectra collected on disordered materials is not trivial due to large static disorder and non-Gaussian pair distributions (e.g. see Brown et al., 1995), this paper particularly focuses on a procedure for deriving reliable structural parameters for REE in quenched melts. To account for anharmonicity induced by the disorder, we applied a gamma-like distribution function to model the Y–O pair correlation of the first coordination shell.

1.1. EXAFS analysis in disordered materials

The EXAFS signal is caused by back scattering of photoelectrons from neighboring atoms of the absorbing element in the structure and thus provides element-specific and quantitative information on the number of neighbors and interatomic distance (see e.g. Brown et al. (1995) for an introduction to EXAFS on glasses and melts). To derive this structural information from EXAFS, the data have to be fitted to a structural model. For ordered structures such as most crystalline materials, a harmonic approach based on symmetric Gaussian pair correlations can be used (Stern, 1974). This harmonic approach takes also into account small thermal and structural disorder, represented by the Debye–Waller factor (Sevillano et al., 1979), which describes the mean-square displacement of the atom by thermal or structural vibrations. If the static or thermally induced disorder increases, such as in melts, the harmonic approximation usually fails due to considerably asymmetric pair correlations or anharmonic vibrations. In such cases, analysis of the EXAFS based on a harmonic approximation usually leads to systematic underestimation of interatomic distances and coordination numbers (Brown et al., 1995). However, there are several ways to describe anharmonicity and asymmetry in the pair distribution caused by thermal or structural disorder. The simplest way is to model structural disorder for a single coordination shell and to split the contribution for that shell, which may account for very different interatomic distances in highly distorted coordination polyhedra (Teo, 1986). However, this is usually limited due to Nyquist's sampling theorem,[1] because every sub-shell will add more variables to the fit. For moderate structural or thermally induced anharmonic vibrations the cumulant expansion method (Bunker, 1983; Fornasini et al., 2001) may be used to describe the deviation from a Gaussian pair distribution in terms of additional cumulants. The cumulants parameterize the distribution of interatomic distances and can be connected to the force constants of an effective pair potential (Stern et al., 1991). The cumulant approach, however, becomes inaccurate if the disorder becomes too large or the distribution too asymmetric, which is, unfortunately, the case for glasses and melts in particular. Farges and Brown (1996) used an empirical model to describe the anharmonicity. They extracted the thermally induced anharmonicity for Ni from high-temperature measurements on crystalline compounds and developed a relatively simple expression for correcting the phase term as a function of temperature. Their correction is based on the linear thermal expansion coefficient by Hazen and Finger (1982). Rossano et al. (2000) show in a combined study by EXAFS and MD-simulations that reliable parameters for Fe^{2+} could be achieved by applying a asymmetric pair distribution function (PDF) based on a Gamma-like distribution employing the GNXAS code (Filipponi et al., 1995) .

To describe the structural environment around trace elements in our glasses in an adequate way, we used a histogram-fit with equidistant bins placed over the range of a pair distribution. Each bin is treated as a single scattering path that is weighted by its contribution to a distribution function at that grid point. The shape of the overall histogram fit is defined by an asymmetric distribution function, which is based on the Gamma function (D'Angelo et al., 1994; Filipponi, 2001):

$$P(R) = N_c \frac{\sqrt{p}}{\sigma\ \Gamma(p)} \left[p + \left(\frac{R-R_c}{\sigma}\right)\sqrt{p}\right]^{p-1} \exp\left[-p - \left(\frac{R-R_c}{\sigma}\right)\sqrt{p}\right] \quad (1)$$

with $p = 4/\beta^2$. N_c and R_c represent the number of neighbors and their average distance, respectively. σ and β are the variance, and skewness of the distribution. The distribution is defined for $\beta(R-R_c) > -2\sigma$ (with $P(R) = 0$ elsewhere). $\Gamma(p)$ is Euler's Gamma function.

In practice, the ARTEMIS software (Ravel and Newville, 2005) treats every bin as a single scattering path. The amplitude and the phase were calculated with FEFF6 (Mustre de Leon et al., 1991; Zabinsky et al., 1995). Bins with an incremental distance of 0.05 Å were used and during the fit only the height of each bin is fitted. For every path the amplitude reduction factor S_0^2 was replaced by Eq. (1) and the degeneracy N was set to 1. The Debye–Waller factor σ^2 was set to 0 and the ΔR was set to the difference between position of the bin and the reference bond length used. ΔE_0 is the deviation from the theoretical Fermi level. The resulting $\chi(k)$ for every path were summed up and normalized by the sum of the bin population. This fit procedure results in an approximation of the contribution of a single atom distributed over the distribution given by the histogram (Yevick and Frenkel, 2010; Price et al., 2012).

2. Experimental

2.1. Model compounds

The model compounds were selected to represent a broad range of possible local oxygen coordination environments around Y. Table 1 lists the crystalline model compounds used for characterizing the various coordination environments. With increasing coordination number, the range and the distribution of the bond lengths also increase. All model compounds are commercially available (99.99% metal purity).

2.2. Glass synthesis

The glass compositions by Prowatke and Klemme (2005) (named PK-glasses in the following) were synthesized from oxides (SiO_2 (99.6%); Al_2O_3 (99.99%); TiO_2 (99.99%); metal purity sourced from Sigma Aldrich) and carbonates (K_2CO_3 (99.999%); Na_2CO_3 (99.995%); $CaCO_3$ (99.95%) purchased from Merck). Reagents were mixed in appropriate proportions and ground with acetone in an agate mortar for homogenization. The mixed powders were decarbonated at 1273 K for 4 h and fused in a platinum or platinum–gold crucible at 1873 K and annealed for 48 h at the same temperature with in a Nabertherm© HT04/17 furnace. The crucible was placed in a water bath to quench the melt to a glass. After quenching, the glass was crushed and fused again for 24 h at 1873 K to expedite homogenization. To add trace elements, the glass was ground again under acetone in an agate mortar and mechanically mixed with 5000 ppm of yttrium and gadolinium. These elements were added in form of high-purity Y_2O_3 (99.999%) and

[1] Nyquist's sampling theorem: number of independent parameters in the data $N_{idp} \approx (2\Delta k \Delta R)/\pi$ must be higher than the number of variables.

Table 1
Crystallographic data of the first Y coordination shell for the model compounds. The standard deviation is displayed in brackets.

Chemical formula	Coordination number	Bond length Y–O [Å]	Average distance Y–O [Å]	Reference
Y_2O_3	6	6×2.280 (0.002) 2×2.243 (0.003) 2×2.272 (0.003) 2×2.331 (0.003)	2.280	Kevorkov et al. (1995)
$Y_3Al_5O_{12}$	8	4×2.303 (0.002) 4×2.438 (0.003) 1×2.33 (0.03) 1×2.35 (0.03) 1×2.35 (0.13) 1×2.37 (0.08)	2.372	Dobrzycki et al. (2004)
$YNO_3 \cdot 6H_2O$	9	1×2.44 (0.02) 1×2.46 (0.06) 1×2.50 (0.05) 1×2.51 (0.04) 1×2.55 (0.09)	2.429	Ribar et al. (1980)

Gd_2O_3 (99.999%). The mixed powders were fused again for 24 h in a platinum crucible, followed by water quench. All glasses were free of bubbles and did not show any sign of crystallization under the optical microscope. The color of the glasses varies between transparent to light brown depending on TiO_2 content.

Glass compositions in the system $CaO–Al_2O_3–SiO_2$ (named CAS-glasses in the following) were synthesized from oxides (SiO_2 (99.6%); Al_2O_3 (99.99%); metal purity purchased at Sigma Aldrich) and carbonate ($CaCO_3$ (99.95%) purchased at Merck). To add trace elements, 5000 ppm of yttrium was added in the form of high-purity Y_2O_3 (99.999%). Reagents were mixed in appropriate proportions and ground with acetone in an agate mortar to ensure homogenization. The mixed powders were decarbonated at 1273 K in a platinum crucible for 4 h. To prepare the powder for the final fusing it was pressed to pellets. The pellets were fused at ca. 2000 K in a contact-less furnace based on aerodynamic levitation (using an argon/oxygen flow) with laser heating (CEMHTI, Orleans, France) due to the high melting temperature and/or fast quench needed. Fusing itself takes ca. 30 s and was followed by a quench within 0.5 s. Detailed description of this setup can be found e.g. in Landron et al. (2000). All CAS-glasses were colorless, free of bubbles and didn't show any signs of crystallization under the optical microscope.

All glass pieces were mounted in epoxy, ground and polished first with abrasive paper, followed by a series of diamond pastes down to 0.25 μm. The polished sections were carbon coated and analyzed using an electron microprobe (JEOL JXA-8500F). The major components were analyzed with an acceleration voltage of 15 kV, beam current of 5 nA and enlarged beam diameter of 10 μm. The counting times were 10 s on the peaks of Al, Si, Ti, Ca, and K and 5 s on the background. To minimize effects of Na migration induced by the electron beam, Na was analyzed first and with counting times of 5 s on the peak and 2.5 s on the background. The standards used were albite (Na), orthoclase (K), corundum (Al), periclase (Mg), wollastonite (Ca, Si) and rutile (Ti). The trace elements Y and Gd were analyzed with an acceleration voltage of 15 kV, beam current of 40 nA and counting times of 80 s on peak and 40 s on background with an enlarged beam diameter of 10 μm. For each sample two line scans with 20 points each were measured and the average values are shown in Tables 2 and 3. All samples agreed with the compositions from Prowatke and Klemme (2005) and with those from the MD simulations (Haigis et al., 2013–this issue). The low standard deviation suggests good homogeneity of the glasses in terms of major and trace element. No signs of crystallization were observed by the scanning electron images obtained at the microprobe.

2.3. Sample preparation for EXAFS

The model compounds were ground in an agate mortar to achieve a homogeneous grain size (<50 μm). An appropriate amount of the powdered compound was mixed with cellulose in an agate mortar to reach a dilution level corresponding to the optimum thickness (Tröger et al., 1992; Ravel and Newville, 2005). Each mixture was pressed into a pellet with a diameter of 13 mm and fixed on a kapton tape. The glasses were also ground in an agate mortar and pressed into a sample holder made of polymethyl methacrylate (PMMA) with a thickness of 5 mm and an area of 3×16 mm^2 covered from both sides with kapton tape.

2.4. Acquisition of EXAFS spectra

EXAFS spectra at the Y K-edge (17,038 eV) were collected at the Hamburger Synchrotronstrahlungslabor (DESY, Hamburg, Germany), on the bending magnet beamline *C*. The storage ring operating conditions of DORIS III were 4.5 GeV electron energy and 80–120 mA positron current. A Si(111) fixed-exit two-crystal monochromator was used. The beamsize was 1.5 mm vertical and 8 mm in the horizontal direction (Rickers et al., 2007). The second crystal of the monochromator was detuned to 50% of the intensity to suppress higher harmonics. The incident and transmitted beam intensities were monitored with two ionization chambers using Ar and Kr as absorbing gas, respectively. To collect spectra in transmission mode the sample was placed between the first and second ion chamber perpendicular to the beam. In fluorescence mode the sample was turned to 45° to the beam and the signal was collected using a Stern–Heald type detector (Lytle et al., 1984) perpendicular to the beam. For all scans, a reference foil (Y metal, 25 μm thick), placed between the second and third ion chamber, was used to provide an accurate internal energy calibration of the monochromator. The angle of the monochromator was measured using Heidenhain encoders. For the model compounds, spectra were recorded in transmission mode between 250 eV below and up to 1200 eV above the absorption edge. For the glass samples, spectra were collected in fluorescence mode

Table 2
Major element composition (wt.%) and trace element content of the PK-glasses with calculated CIPW-norm[a] and ASI.[b] The standard deviation is displayed in brackets.

Comp.	ASI200	ASI220	ASI240	ASI250	ASI260	ASI280
K_2O	0.90 (0.07)	1.06 (0.07)	1.30 (0.07)	1.38 (0.09)	1.31 (0.08)	1.18 (0.06)
Na_2O	11.55 (0.33)	11.01 (0.32)	10.35 (0.29)	9.61 (0.32)	8.34 (0.32)	5.72 (0.23)
CaO	10.78 (0.20)	8.55 (0.19)	6.23 (0.14)	5.25 (0.16)	5.20 (0.13)	8.70 (0.21)
TiO_2	11.81 (0.20)	8.22 (0.20)	4.70 (0.15)	3.25 (0.16)	3.06 (0.13)	4.31 (0.15)
Al_2O_3	4.78 (0.12)	9.32 (0.15)	15.03 (0.25)	17.47 (0.21)	19.06 (0.15)	20.43 (0.20)
SiO_2	58.29 (0.42)	60.39 (0.36)	62.19 (0.42)	62.31 (0.51)	61.70 (0.44)	58.20 (0.38)
ASI	0.115	0.258	0.481	0.636	0.755	0.768
Gd_2O_3	0.57 (0.02)	0.55 (0.09)	0.49 (0.02)	0.52 (0.02)	0.54 (0.01)	0.50 (0.01)
Y_2O_3	0.57 (0.04)	0.58 (0.04)	0.43 (0.01)	0.46 (0.01)	0.49 (0.04)	0.50 (0.04)
Qz	20.89	12.42	0.37	–	0.29	5.35
Or	5.32	6.26	7.68	8.16	7.74	6.97
Ab	19.58	42.04	70.07	77.08	81.27	74.98
Ns	18.19	11.90	4.08	–	–	–
Wo	5.16	5.76	6.07	–	1.85	0.66
Ti	28.98	20.17	11.53	–	7.51	10.58
Pf	–	–	–	5.53	–	–
Ne	–	–	–	2.54	–	–

[a] CIPW-norm: calculation of normative mineral compositions (Johannsen, 1931), Qz = quartz (SiO_2), Or = orthoclase ($KAlSi_3O_8$), Ab = albite ($NaAlSi_3O_8$), Ns = natriumdisilicate, Wo = wollastonite ($CaSiO_3$), Ti = titanite($CaTiSiO_5$), Pf = perovskite ($CaTiO_3$), Ne = nepheline ($NaAlSiO_4$).

[b] ASI: molar radio of $Al_2O_3/(Na_2O + K_2O + CaO)$; indicates degree polymerization (Zen, 1986).

Table 3
Major element composition (wt.%) and trace element content of the CAS-glasses. The standard deviation is displayed in brackets.

Comp.	$CaSiO_3$	$Ca_3Al_2Si_3O_{12}$	$CaAl_2Si_2O_8$
CaO	48.28 (0.20)	38.04 (0.19)	20.79 (0.14)
SiO_2	51.05 (0.27)	39.17 (0.22)	42.10 (0.21)
Al_2O_3	–	22.18 (0.14)	36.50 (0.16)
Y_2O_3	0.59 (0.02)	0.61 (0.02)	0.61 (0.02)

between 250 eV below and up to 900 eV above the edge. An average of 2 acquisitions (model compounds) and of 6–8 acquisitions (glasses) were collected in order to reach sufficient counting statistics and an adequate signal to noise ratio.

2.5. EXAFS analysis

The EXAFS spectra were extracted using the AUTOBK algorithm (Newville, 2001) that is part of the ATHENA software (Ravel and Newville, 2005). For background subtraction and normalization, a Victoreen function was used in the pre-edge region, −200 eV to −30 eV relative to the edge and a spline function in the post-edge region, i.e. 150 eV to 975 eV relative to edge for the model compounds and 150 eV to 800 eV for the glasses. The edge position, E_0 for all spectra was set to the half-height of the edge step. To remove the low frequency background the Rbkg value in AUOTBK was set to 1.2 Å. The k^3-weighted EXAFS signal was Fourier transformed over the range of 3–15 $Å^{-1}$ for the model compounds and over the range of 3–13.5 $Å^{-1}$ for the glasses using a Kaiser–Bessel window.

To fit the spectra of the model compounds, a harmonic approach was used based on a Gaussian function. This approach results in four parameters for each fitted pair correlation: N, R, σ^2 and ΔE_0, which represent the number of neighbors, the average bond length, the Debye–Waller factor and the deviation from the theoretical Fermi level. The amplitude and atomic phase-shift were theoretically calculated with FEFF6 (Mustre de Leon et al., 1991; Zabinsky et al., 1995) using the ARTEMIS software package (Ravel and Newville, 2005). To check, if the histogram fit based on the Gamma-function produces reliable values also for Gaussian pair distributions, the first coordination shell for model compounds was also fitted with the histogram fit function, whereas higher coordination shell contributions were fitted with the harmonic model. The main purpose of the model compounds is to check if the theoretically calculated phase shift and the amplitude can be used to fit the measured data in an adequate way, which is indicated by small values of ΔE_0 and a good representation of known crystallographic parameters.

For the glasses, the histogram fit based on the asymmetric distribution function was used to determine the structural parameters of the first coordination shell. The histogram fit for the first shell was combined with a fit of two Gaussian distributions for the second shell. The main purpose for including the second shell is to improve the fit quality of the first coordination shell. This is likely due to the fact that the first and second coordination shell overlap considerably due to the high configurational disorder in the system, so that the signals of the two shells cannot be well separated by Fourier filtering of the EXAFS.

3. Results

3.1. Model compounds

Spectra of model compounds were fitted based on structural data from the literature (Table 1) using both the Gaussian and the asymmetric fit model for the first coordination shell. The EXAFS-derived local structural parameters are shown in Table 4. Only those shells were included, which have shown a significant contribution to the total EXAFS. The k^3-weighted EXAFS spectra of the model compounds, the corresponding Fourier transforms (FT) and the fit are shown in Fig. 1A and B. For Y_2O_3 the EXAFS spectrum shows strong oscillations up to 15 $Å^{-1}$. The corresponding FT shows four maxima. The maxima can be assigned to the first O coordination shell as well as to two Y–Y and one mixed Y–O, Y–Y pair correlations for higher coordination shells. Y is located in two sites in this cubic structure (space group Ia-3). One represents a regular octahedron with six O at a distance of 2.280 Å whereas the other represents a distorted octahedron with 3×2 O at 2.243 Å, 2.272 Å and 2.331 Å, resulting in an average distance of 2.280 Å for the first shell (distances are taken from the crystal structure; Kevorkov et al., 1995). For the fit of the first shell (Y–O) four different path contributions were included. Therefore, two separate FEFF calculations were made, one where Y is represented by a regular octahedron with one bond length only and the second where Y is coordinated in a distorted octahedron with three different bond lengths (see Table 1). For the second ($Y-Y_1$), third ($Y-O_3$, $Y-O_2$, and $Y-Y_2$) and fourth ($Y-Y_3$) shell one path length for each contribution was included (see Fig. 1B). All coordination numbers were fixed to the value of the crystal structure. In the second fitting cycle, ΔE_0 was fixed during the fit to minimize the standard deviation for the R, σ^2 and C_3 respectively R, σ and β. The derived average bond length is in good agreement with the average bond length from the model crystal structure. In comparison, the fit of the first coordination shell with the histogram fit results in similar values for the average bond length (see Table 4). For both fit models, the good quality of the fit is supported by the small R-

Table 4
Structural parameters determined by the fit of the EXAFS for Y in the model compounds. Standard deviation for each value is listed in brackets. * indicates the parameters fixed during the fit.

Value	Y_2O_3-Gaussian	Y_2O_3-Histo	$Y_3Al_5O_{12}$-Gaussian	$Y_3Al_5O_{12}$-Histo
R-factor	0.014	0.011	0.008	0.010
Red. χ^2	279.53	248.43	165.4	189.6
ΔE_0	−1.4 eV*	−1.2 eV*	1.1 eV*	−1.4 eV*
N_{Y-O}	6*	6*	8*	8*
R_{Y-O}	2.28 Å (0.01)	2.28 Å (0.01)	2.37 Å (0.01)	2.38 Å (0.01)
σ^2_{Y-O}	0.005 (0.001)	–	0.004 (0.001)	–
σ_{Y-O}	–	0.080 (0.005)	–	0.110 (0.004)
β_{Y-O}	–	0.50 (0.35)	–	0.40 (0.01)
N_{Y-Y1}	6*	6*	N_{Y-Al21} 3*	3*
R_{Y-Y1}	3.53 Å (0.01)	3.53 Å (0.01)	R_{Y-Al21} 3.03 Å (0.03)	3.02 Å (0.01)
σ^2_{Y-Y1}	0.004 (0.001)	0.004 (0.001)	σ^2_{Y-Al21} 0.005 (0.001)	0.005 (0.001)
N_{Y-Y2}	6*	6*	N_{Y-Al1} 4*	4*
R_{Y-Y2}	4.00 Å (0.01)	4.00 Å (0.01)	R_{Y-Al1} 3.38 Å (0.02)	3.36 Å (0.01)
σ^2_{Y-Y2}	0.007 (0.001)	0.008 (0.001)	σ^2_{Y-Al1} 0.005 (0.001)	0.005 (0.001)
N_{Y-O1}	6*	6*	N_{Y-Al22} 3*	3*
R_{Y-O1}	4.48 Å (0.02)	4.46 Å (0.02)	R_{Y-Al22} 3.71 Å (0.03)	3.68 Å (0.01)
σ^2_{Y-O1}	0.004 (0.001)	0.004 (0.004)	σ^2_{Y-Al22} 0.005 (0.001)	0.005 (0.001)
N_{Y-O2}	6*	6*	N_{Y-Y1} 4*	4*
R_{Y-O2}	4.15 Å (0.02)	4.15 Å (0.01)	R_{Y-Y1} 3.69 Å (0.01)	3.68 Å (0.01)
σ^2_{Y-O2}	0.002 (0.002)	0.005 (0.004)	σ^2_{Y-Y1} 0.004 (0.001)	0.005 (0.001)
N_{Y-Y3}	6*	6*	N_{Y-O1} 8*	8*
R_{Y-Y3}	5.33 Å (0.01)	5.33 Å (0.01)	R_{Y-O1} 3.88 Å (0.05)	3.82 Å (0.01)
σ^2_{Y-Y3}	0.007 (0.001)	0.007 (0.001)	σ^2_{Y-O1} 0.002 (0.001)	0.003 (0.002)

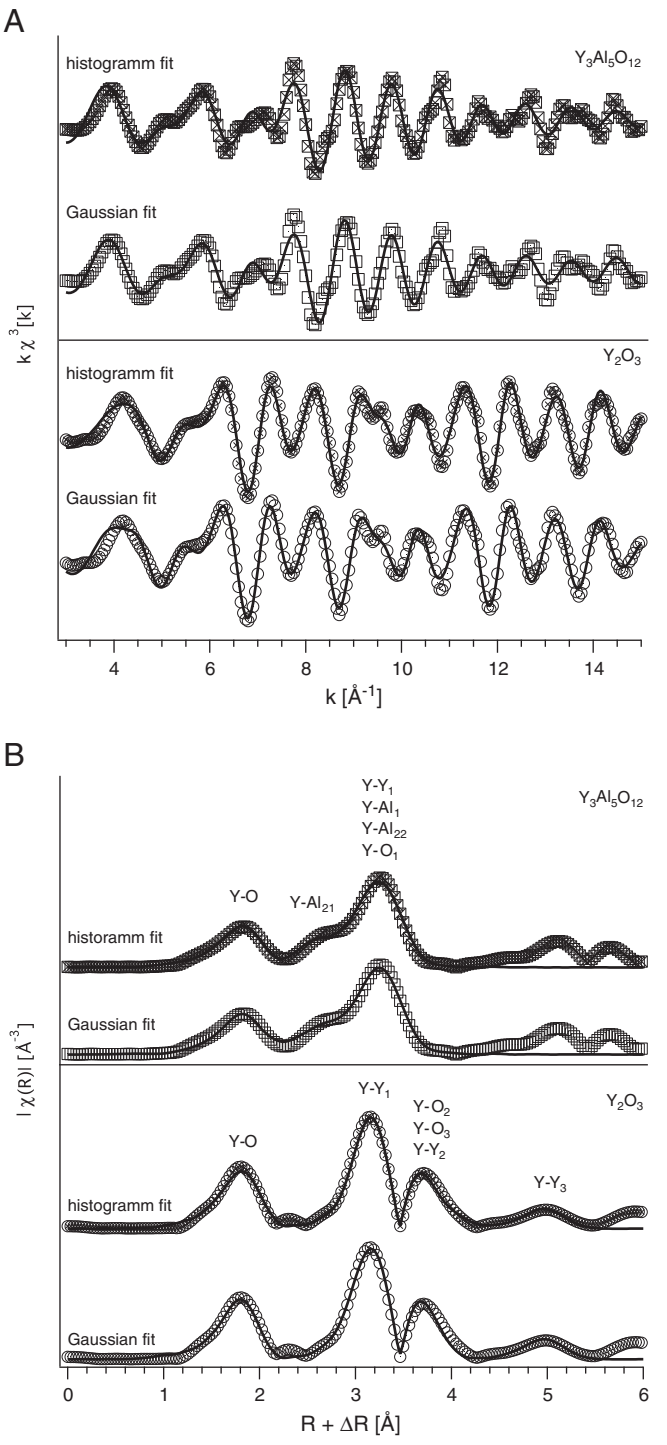

Fig. 1. A: k^3-weighted Y-EXAFS for Y_2O_3 and $Y_3Al_5O_{12}$. Markers indicate the data points and solid lines the respective fits. B: FT's of the Y-EXAFS for Y_2O_3,and $Y_3Al_5O_{12}$. Markers indicate data points and solid lines the respective fits. Peaks in the FT are labeled for the corresponding atomic pair correlations. Peaks with more than one label indicate overlap of pair correlations. Peak positions are uncorrected for backscattering phase-shifts.

factor, the small red. χ^2 and the small values of ΔE_0, the deviation from the theoretical Fermi level.

For $Y_3Al_5O_{12}$, the EXAFS spectrum shows clear oscillations up to 15 Å^{-1}, with slight damping starting at 11 Å^{-1}. The FT shows two maxima that can be assigned to the first O coordination shell and the second coordination shell, which consists of contributions Y–Al, Y–O, and Y–Y pair correlations. The two maxima at 5.2 Å and 5.7 Å (uncorrected for phase shift) are difficult to assign, because of too many different path contributions. They could be related to multiple scattering paths as well as to higher shell pair correlations. For the first coordination shell, Y is located in a slightly distorted dodecahedral site with four O at 2.309 Å and four O at 2.381 Å, which yield an average distance of 2.35 Å for the first shell (Table 1). For the fit of the first shell (Y–O) two path contributions were included with two different bond lengths (see Table 1). For the fit of the second shell, five path contributions (Y–Al_{21}, Y–Al_{22}, Y–Al_1, Y–O_1, and Y–Y_1) each with one bond length were included (see Fig. 2). All coordination numbers were set to the value of the crystal structure. In the second fitting cycle, ΔE_0 was fixed during the fit to minimize the standard deviation for the values R, σ^2 and C_3 respectively R, σ and β. The fit results show that the average bond length is in good agreement with the crystallographic data. In comparison, the analysis with the histogram fit results in similar values for the average bond length (see Table 4). For both fit models, the good quality of the fit is supported by the small R-factor, the small red. χ^2 and the small values of ΔE_0.

In Fig. 2 the average bond length is plotted versus the coordination number for Y_2O_3, $Y_3Al_5O_{12}$ and $YN_3O_9{\cdot}6H_2O$. For Y_2O_3, $Y_3Al_5O_{12}$, values from the structure database and those derived by the fit of the EXAFS are shown. For $YN_3O_9{\cdot}6\,H_2O$, only the value of the structure database is shown. Because of dehydration of the sample during beam exposure, spectrum acquisition was not possible. Nonetheless, there is a linear relationship between coordination number and average bond length. This relationship will be further used as a first-order constraint to estimate the coordination number of Y in the glasses from the Y–O distance.

3.2. Glasses

The k^3-weighted EXAFS spectra of all glasses and the corresponding FTs are shown in Figs. 3 and 4 together with the resulting fit. At first sight, the EXAFS spectra of the PK-glasses as well as CAS-glasses look quite similar in terms of the wavelength of the oscillations. However, the amplitude decreases considerably from ASI200 to ASI280 (Fig. 3A) as well as from $CaSiO_3$ to $CaAl_2Si_2O_8$ (Fig. 4A). The position of the first maximum of the FT, which corresponds to the Y–O correlation of the first coordination shell, shift from 1.75 Å for ASI 200 to 1.65 Å for ASI280 and 1.75 Å for $CaSiO_3$ to 1.69 Å for $CaAl_2Si_2O_8$ (all positions reported here are not corrected for phase shift). The first maximum,

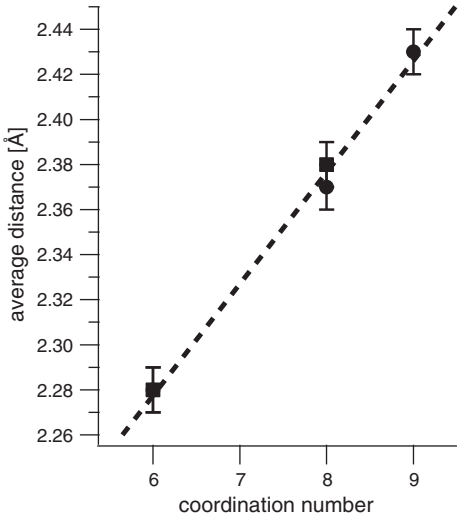

Fig. 2. O coordination number of Y, plotted against Y – O bond length for measured model compounds. Circles indicate the values taken from the crystal structure; squares indicate the values are taken from the EXAFS fit.

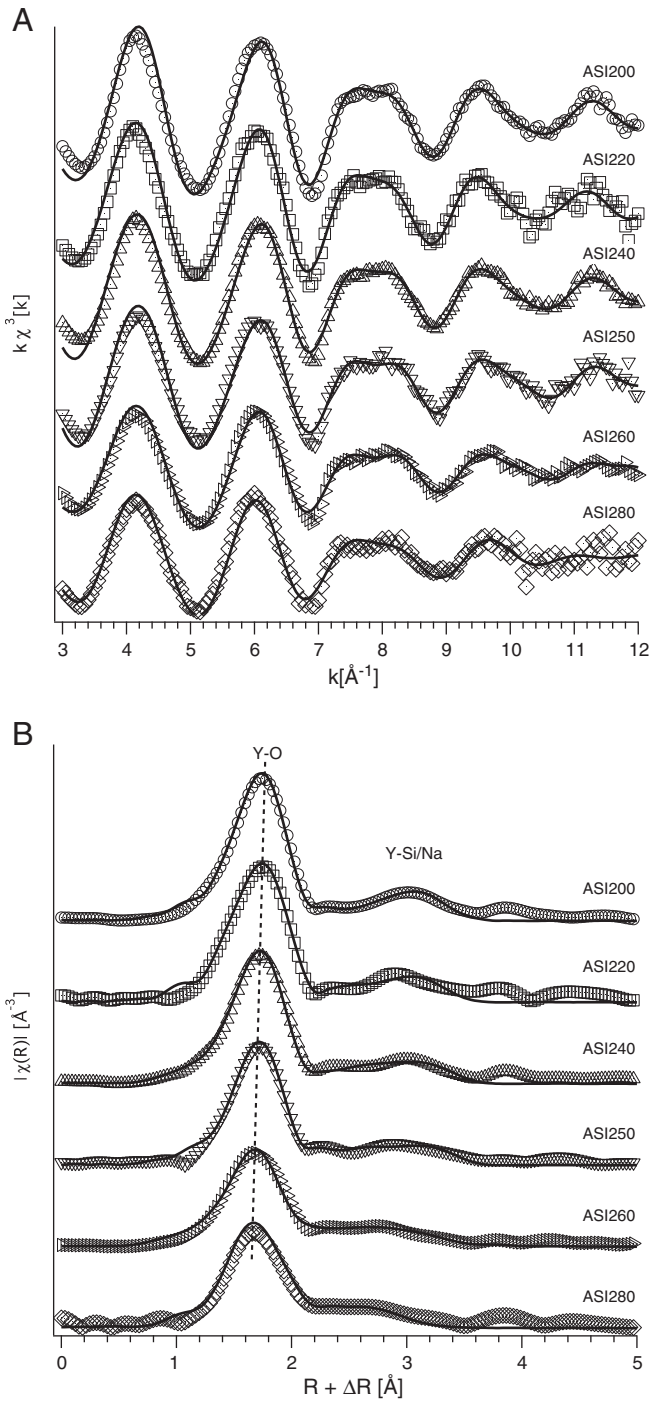

Fig. 3. A: k^3-weighted Y-EXAFS spectra for PK-glasses ASI200, ASI220, ASI 240, ASI250, ASI260 and ASI280. Markers indicate the data points and solid lines the respective fits. B: FT's of the Y-EXAFS for ASI200, ASI220, ASI 240, ASI250, ASI260 and ASI280. Markers indicate data points and solid lines the respective fits. Peaks in the FT are labeled for the corresponding pair correlations. Peak positions are uncorrected for backscattering phase-shifts.

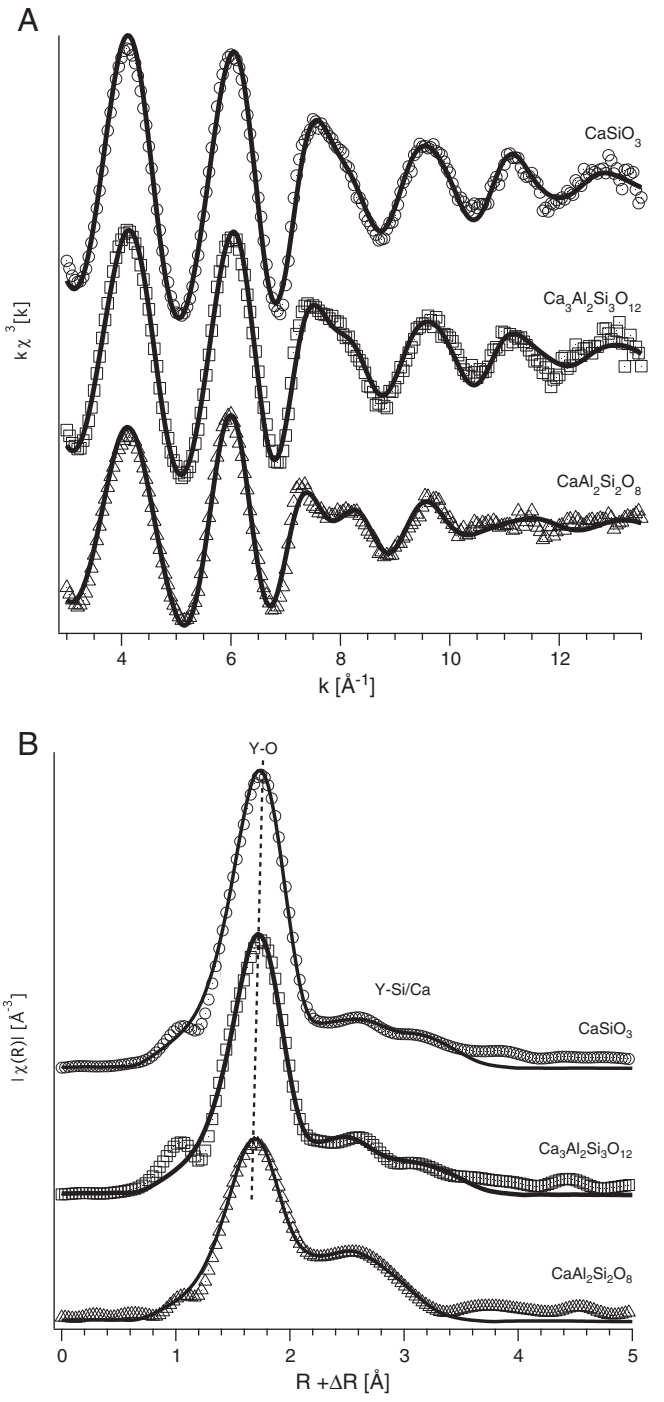

Fig. 4. A: k^3-weighted Y-EXAFS spectra for glass samples $CaSiO_3$, $Ca_3Al_2Si_3O_{12}$ and $CaAl_2Si_2O_8$. Markers indicate data points and solid lines the respective fits. B: FT's of the Y-EXAFS for $CaSiO_3$, $Ca_3Al_2Si_3O_{12}$ and $CaAl_2Si_2O_8$. Markers indicate data points and solid lines the respective fits. Peaks in the FT are labeled for the corresponding pair correlations. Peak positions are uncorrected for backscattering phase-shifts.

however, shows a considerable decrease in the magnitude from 5.26 arb. units for ASI200 to 3.49 arb. units for ASI280 and 4.64 arb. units for $CaSiO_3$ to 2.89 arb. units for $CaAl_2Si_2O_8$ and significant increase of broadening from ASI200 to ASI280 (Fig. 3B) as well as from $CaSiO_3$ to $CaAl_2Si_2O_8$ (Fig. 4B). The second maximum of the FT corresponds to pair correlations of the second coordination shell. For the PK-glasses, the magnitude decreases from 1.04 arb. units for ASI200 to 0.79 arb. units for ASI280. For the CAS-glasses, the magnitude slightly increases from 0.80 arb. units for $CaSiO_3$ to 1.11 arb. units for $CaAl_2Si_2O_8$. In addition, a slight shift of this maximum to lower distances is observed from 2.98 Å for ASI200 to 2.61 Å for ASI280 and also from 2.64 Å for $CaSiO_3$ to 2.58 Å for $CaAl_2Si_2O_8$.

The structural parameters for the glass samples obtained from the fit are shown in Table 5 (PK-glasses) and Table 6 (CAS-glasses). The spectra were modeled by combining the histogram fit based on the gamma-like distribution for the first coordination shell with a fit of two Gaussian distributions for the second coordination shell. When we used the histogram fit also for the second coordination shell, no stable fit could be obtained. Attempts to fit only the first coordination

shell using the filtered signal corresponding to the first maximum of the FT yielded only low quality fits for the Y–O correlation. This is likely due to the fact that the first and second coordination shells overlap considerably. Therefore, the signals of the two shells cannot be well separated in the FT. The parameters N_{Y-O}, σ and β of the first shell are strongly correlated. The same holds for the parameters N_{Y-Si} and N_{Y-Na} of the second shell with their respective σ^2 parameters. In order to obtain physically meaningful parameters, the average coordination numbers had to be fixed during the fit. After a first fitting cycle with N_{Y-O} set to 6, the parameter N_{Y-O} was evaluated based on the determined average Y–O distance using the correlation between distance and coordination number shown in Fig. 2 and adjusted accordingly. In the second fitting cycle, ΔE_0 was fixed during the fit, to minimize the standard deviation for the values R, σ and β. The resulting Y–O pair distribution functions are shown for the PK glasses in Fig. 5 and for the CAS-glasses in Fig. 6. For all samples the maximum of the distribution is at ca. 2.25 Å. The Y–O pair distributions of the ASI200, ASI220 glass and the $CaSiO_3$ glass are almost symmetric. The four other PK-glasses show considerable asymmetry in the pair distribution reflected by the β-parameter, which changes from 0.40 ± 0.01 for ASI200 to 1.00 ± 0.16 for ASI280. The two other CAS-glasses also display significant asymmetry in the pair distribution. For these samples, the β-parameter changes from 0.40 ± 0.01 for $CaSiO_3$ to 0.68 ± 0.01 for $Ca_3Al_2Si_3O_{12}$. Furthermore, the width of the distribution increases considerably from 0.093 ± 0.004 for ASI200 to 0.206 ± 0.023 for ASI280 and from 0.105 ± 0.003 for $CaSiO_3$ to 0.154 ± 0.009 for $CaAl_2Si_2O_8$. The change in the width and asymmetry of the pair distribution function causes remarkable changes in the average Y–O distance although the maximum of the distribution is nearly constant. The average Y–O distance is 2.27 ± 0.01 Å for ASI200, ASI220, ASI240, 2.28 ± 0.01 Å for ASI250, 2.32 ± 0.01 Å for ASI260 and 2.40 ± 0.02 Å was fitted for ASI280. For the CAS glasses the obtained average Y–O distance changes from 2.28 ± 0.01 Å for $CaSiO_3$ to 2.31 ± 0.01 Å for $Ca_3Al_2Si_3O_{12}$ and to 2.34 ± 0.01 Å for $CaAl_2Si_2O_8$. Using the correlation shown in Fig. 2, the distances are consistent with an average coordination number of 6 for ASI200, ASI220, ASI240, and ASI250, whereas the value of ASI260 indicates a coordination number of 7 and the one of ASI 280 a coordination number of 8. The uncertainty of the average coordination numbers obtained from EXAFS is usually quite high and estimated to be at least ± 0.5 (Brown et al., 1988) However, the fit of ASI260 with $N_{Y-O} = 7$ shows an improved R-factor ($R = 0.012$) and reduced-χ^2 (red. $\chi^2 = 33.8$) parameter compared to $N_{Y-O} = 6$ ($R = 0.013$, red. $\chi^2 = 36.7$). Similarly, ASI 280 better fitted with $N_{Y-O} = 8$ ($R = 0.007$, red. $\chi^2 = 3.2$) compared to the fit with $N_{Y-O} = 7$ ($R = 0.007$, red. $\chi^2 = 3.7$). In our view, these differences support the higher average Y coordination number for these samples. The Y average coordination numbers for the CAS glasses obtained from the molecular dynamics simulation by Haigis et al. (2013–this issue) show a very similar systematic trend, compared to those obtained by EXAFS for the PK-glasses, i.e. 6.2 for $CaSiO_3$, 6.6 for $Ca_3Al_2Si_3O_{12}$, and 6.9 for $CaAl_2Si_2O_8$. In case of the CAS-glasses, the Y average coordination numbers were fixed to the values obtained of the MD simulation by Haigis et al. (2013–this issue).

The second coordination shell shows a weak but non-negligible contribution to the EXAFS signal. For the analysis, the second coordination shell was described by mixing contributions of Si and Na for the PK-glasses and Si and Ca for the CAS-glasses. Si and Al are not distinguishable and abundances of other elements are probably too low. The resulting average coordination numbers are quite low and do not vary significantly. The second coordination shell in glasses is usually characterized by strong positional disorder leading to broad and asymmetric pair correlations (cf. e.g. Haigis et al., 2013–this issue), Therefore, these apparently low average coordination numbers are probably related to the simplicity of the used fit model and particularly the absolute value of the parameters should be treated with caution. Hence, we will not further discuss the results obtained for the second shell. As explained earlier, fitting of the second coordination shell was primarily included to improve the results for the Y–O shell.

Table 5
Structural parameters determined by the fit of the EXAFS for Y in the PK-glasses ASI200, ASI220, ASI240, ASI250, ASI260 and ASI280. The standard deviation is displayed in brackets. * indicates the parameters fixed during the fit.

Value	ASI200	ASI220	ASI240	ASI250	ASI260	ASI280
R-factor	0.006	0.004	0.008	0.0010	0.011	0.007
Red. χ^2	39.2	8.2	47.5	16.7	33.8	3.2
ΔE_0	−2.2 eV*	−3.4 eV *	−0.8 eV*	−1.3 eV*	−1.0 eV*	−1.3 eV*
N_{Y-O}	6*	6*	6*	6*	7*	8*
R_{Y-O}	2.27 Å (0.01)	2.27 Å (0.01)	2.27 Å (0.01)	2.27 Å (0.01)	2.32 Å (0.01)	2.40 Å (0.02)
σ_{Y-O}	0.093 (0.004)	0.098 (0.003)	0.100 (0.004)	0.108 (0.004)	0.148 (0.010)	0.206 (0.023)
β_{Y-O}	0.04 (0.01)	0.04 (0.01)	0.41 (0.24)	0.44 (0.22)	0.84 (0.16)	1.00 (0.16)
N_{Y-Si}	2*	2*	3*	2*	2*	1*
R_{Y-Si}	3.83 Å (0.04)	3.85 Å (0.03)	3.83 Å (0.07)	3.80 Å (0.03)	3.52 Å (0.05)	3.65 Å (0.02)
σ^2_{Y-Si}	0.008 (0.002)	0.007 (0.001)	0.016 (0.003)	0.009 (0.002)	0.011 (0.003)	0.004 (0.001)
$c3_{Y-Si}$	0.008 (0.001)	0.009 (0.001)	0.008 (0.002)	0.007 (0.001)	0.002 (0.001)	0.004 (0.001)
N_{Y-Na}	4*	3*	3*	2*	2*	4*
R_{Y-Na}	3.57 Å (0.04)	3.57 Å (0.03)	3.57 Å (0.05)	3.54 Å (0.0)	2.60 Å (0.04)	2.89 Å (0.02)
σ^2_{Y-Na}	0.011 (0.001)	0.009 (0.001)	0.010 (0.002)	0.008 (0.002)	0.011 (0.003)	0.017 (0.002)
$c3_{Y-Na}$	0.001 (0.001)	−0.001 (0.001)	−0.001 (0.001)	−0.001 (0.001)	−0.005 (0.001)	0.006 (0.001)

Table 6
EXAFS determined parameters for Y in $CaSiO_3$, $Ca_3Al_2Si_3O_{12}$ and $CaAl_2Si_2O_8$ glasses. The standard deviation is displayed in brackets. * indicates the fixed parameters during the fit.

Value	$CaSiO_3$	$Ca_3Al_2Si_3O_{12}$	$CaAl_2Si_2O_8$
R-factor	0.006	0.006	0.006
Red. χ^2	39.2	27.0	43.5
ΔE_0	−2.2 eV*	−1.6 eV*	−1.0 eV*
N_{Y-O}	6.2*	6.6*	6.9*
R_{Y-O}	2.28 Å (0.01)	2.31 Å (0.01)	2.34 Å (0.01)
σ_{Y-O}	0.105 (0.003)	0.124 (0.005)	0.154 (0.009)
β_{Y-O}	0.40 (0.12)	0.64 (0.13)	0.68 (0.15)
N_{Y-Ca}	1*	2*	4*
R_{Y-Ca}	2.90 Å (0.04)	2.91 Å (0.03)	2.99 Å (0.04)
σ^2_{Y-Ca}	0.011 (0.001)	0.016 (0.001)	0.022 (0.003)
$c3_{Y-Ca}$	−0.001 (0.001)	−0.001 (0.001)	0.001 (0.001)
N_{Y-Si}	2*	2*	3*
R_{Y-Si}	3.40 Å (0.03)	3.40 Å (0.05)	3.57 Å (0.05)
σ^2_{Y-Si}	0.013 (0.002)	0.014 (0.002)	0.015 (0.002)
$c3_{Y-Si}$	−0.002 (0.001)	−0.003 (0.001)	0.002 (0.001)

4. Discussion

Crystalline model compounds with known structures provide a basis to test the approach used to derive structural parameters by analysis from the EXAFS, particularly if theoretical phase-shift and amplitude functions are used. The presented analysis here has shown that the fitted parameters of both fit models, based on Gaussian or Gamma function, for Y_2O_3 and $Y_3Al_5O_{12}$ match well the crystallographic parameters from the literature determined by X-ray diffraction techniques. This implies that the phase shift and amplitude calculated by FEFF6 as well as the histogram fit based on the Gamma function are well suited to achieve reliable structural information for Y.

REE in silicate and other melts are network-modifying cations with coordination numbers of six and higher because of their large ionic radius, as confirmed in many studies where REE are major components

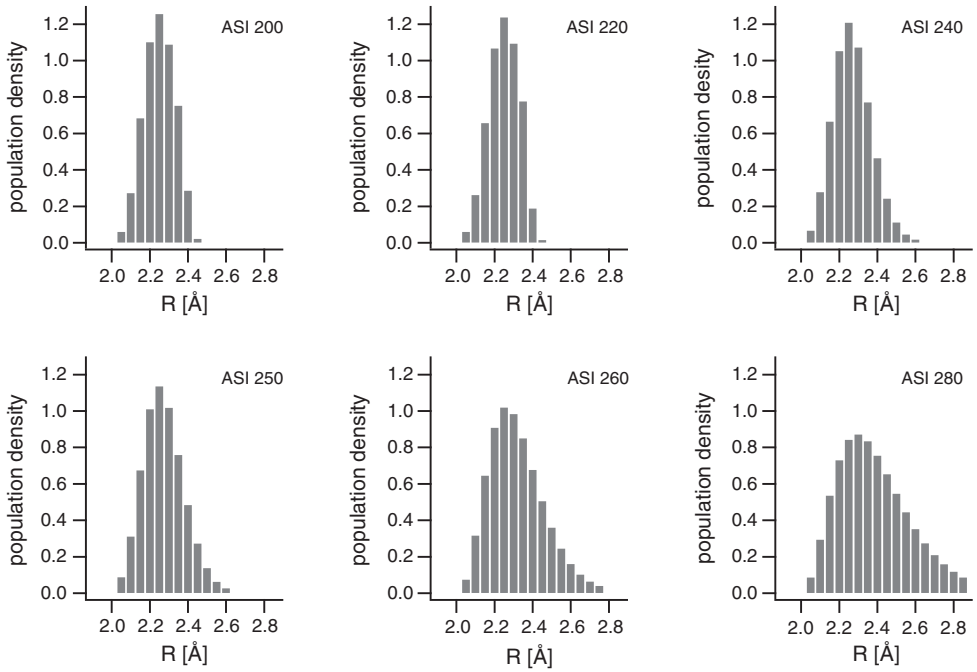

Fig. 5. Y–O pair distribution resulting from the histogram fit for the studied PK glasses as indicated.

(e.g. Sen and Stebbins, 1995; Peters and Houde-Walter, 1997; Anderson et al., 2000; Sen, 2000; Mountjoy et al., 2001; Park et al., 2002; Wilding et al., 2007). To our knowledge there is no comparable study on Y in silicate glasses, but it is usually considered to be a well-suited analog element for the heavy REE due to similar charge and ionic radius (Daane, 1968). The results presented here on Y as a minor component are consistent with the aforementioned results on REE as major components. The results for the PK-glasses show that the average coordination of Y is 6 for glasses with low ASI and increases to 8 as the ASI and polymerization increases. The average bond length increases accordingly from 2.27 ± 0.01 Å to 2.40 ± 0.01 Å. Likewise, a systematic increase is observed for the CAS glasses where the average Y–O distance increases from 2.28 ± 0.01 Å for $CaSiO_3$ to 2.34 ± 0.01 for $CaAl_2Si_2O_8$. Remarkably, the change in the average Y–O distance does not result from overall lengthening of the Y – O bonds, but is attained by an increase of the width and the asymmetry of the Y–O correlation for both suites of samples. Qualitatively, Haigis et al. (2013–this issue) obtained the same trend in the average bond length for the CAS compositions, although the results of the molecular dynamics simulation cannot be directly compared to glasses due to the difference in fictive temperature (for more details see Haigis et al., (2013–this issue). In previous literature, the data set that is best comparable to our new one is the one by Ponader and Brown (1989) on Yb. They report an Yb–O distance of 2.2 Å for the depolymerized sodium–tri-silicate ($Na_2Si_3O_7$, NS3) glass, which decreases to 2.11 Å for the polymerized albitic ($NaAlSi_3O_8$) glass composition. From this change in the distance, a decrease of the coordination number from 6 to 5 was derived. At first sight these results seem to contradict our observations. However, Ponader and Brown (1989) derived the structural parameters based on a symmetric Gaussian distribution function and did not account for anharmonic effects. If the pair distribution is asymmetric this type of analysis usually results in significant underestimation of the interatomic distance and coordination numbers (Brown et al., 1995). In order to be able to better compare Ponader and Brown's (1989) results on Yb with our data on Y, the systematic difference in interatomic distance between Yb and Y for a given coordination number needs to be corrected. This can be done using the tabulated crystal radii by Shannon (1976), which yields a ratio of 1.03 for $^{[6]}$Y and $^{[6]}$Yb. Applying this correction shows that the Yb–O distance of their NS3 composition is consistent with our results for Y in ASI200 and $CaSiO_3$, whereas the one for the albite glass is far off compared to our values for the compositions with the highest degree of polymerization, such as ASI280 and $CaAl_2Si_2O_8$. All EXAFS spectra (La, Gd, and Yb) for the albitic glasses of Ponader and Brown (1989) display a strongly damped EXAFS signal compared to the other glasses. We would like to suggest that this indicates a much larger disorder around the absorber element and considerable anharmonicity, so that the observed decrease in the Yb–O distance and coordination number is rather an artifact of their analysis. First attempts to analyze the spectra presented here using Gaussian pair distributions revealed similar results as observed by Ponader and Brown (1989). Our results based on the histogram fit with

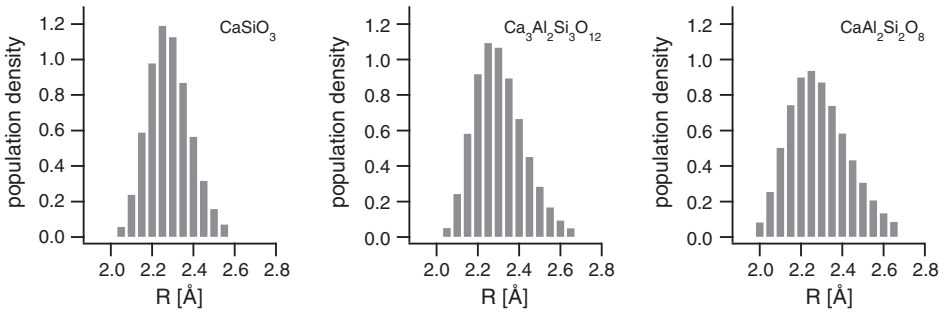

Fig. 6. Y–O pair distribution resulting from the histogram fit for the studied CAS glasses as indicated.

an asymmetric PDF demonstrate that the Y–O pair distribution is more asymmetric and broader for the more polymerized compositions and cannot be approximated by a Gaussian distribution. Our analysis here, particularly the comparison to Yb is further supported by preliminary results from EXAFS spectra collected on Yb for the PK compositions (Simon et al., 2012a).

The structural parameters revealed by our EXAFS analysis can be further tested by analyzing the Y – O bond strength using the empirical bond strength–bond length model first introduced by Brown (1981), which is based on the bond valence concept of Pauling (1929). The bond strength is defined by dividing the formal charge (valence) of an ion by its coordination number. The second Pauling rule states that a stable structure requires that the sum of all bond strengths of a given ion equals the absolute value of its formal charge within ±0.1 valence units (vu). Another way of determining the bond strength s (in valence units; vu) for a given Y – O bond length (R) is to use the empirical relation of Brown and Altermatt (1985):

$$S = \exp\left(\frac{R_0(Y) - R}{0.37\ \text{Å}}\right) \tag{2}$$

in which R_0 (Y) is the ideal bond length and R is the experimentally observed Y–O distance.

Eq. (2) can be combined with the Y–O pair distribution determined by the histogram fit to calculate the bond strength sum for a given configuration around Y, ν_Y (Eq. (3)). For this, the bond strength s_i is determined for each bin i of the histogram fit, weighted by its height h_i and summed up

$$\nu_Y = \sum_{Y-O_i} (S_i * h_i). \tag{3}$$

To derive ν_Y for Y^{3+} we used the R_0 (Y) = 2.019 Å tabulated for $Y^{[6]}$–O (Brown and Altermatt, 1985). For $Y^{[8]}$–O, R_0 (Y) = 2.002 Å was calculated from the crystal structure of $Y_3Al_5O_{12}$ using the program VALENCE (Brown, 1996). The value $R_0(Y)$ = 2.011 Å for $Y^{[7]}$–O was linearly interpolated between those of $Y^{[6]}$–O and $Y^{[8]}$–O because no crystal structure for $Y^{[7]}$ is available.

For the PK-glasses, the calculated bond strength sums ν_Y are equal to 3.02 vu for ASI200, 2.94 vu for ASI220, 3.14 vu for ASI240, 3.13 vu for ASI250 and 3.17 vu for ASI260 and 3.12 vu for ASI 280. For the CAS-glasses ν_Y values are 3.13 vu for $CaSiO_3$, 3.12 vu for $Ca_3Al_2Si_3O_{12}$, and 3.08 vu for $CaAl_2Si_2O_8$. Particularly, the value derived for ASI260 slightly exceeds the value of 3 ± 0.1 vu required by Pauling's second rule. This could be explained by the fact that we used only an interpolated value R_0 (Y) for 7-fold coordinated Y.

Y in 6-fold coordination can only bond to non-bridging oxygens in order not to exceed the maximum value of 2 vu for the sum of bond strengths for the oxygens involved. In order to maintain this maximum value, bonding of $^{[6]}$Y to bridging oxygens would imply considerable lengthening of the involved (Si, Al) – O bonds and disruption of the tetrahedral network, which is rather unlikely and not supported by any experimental evidence. It is also unlikely that $^{[6]}$Y preferentially bonds to oxygens of Al–O–Al linkages. Although theoretically possible, this would contradict the observed increase of crystal–melt partition coefficients with increasing ASI (Prowatke and Klemme, 2005). Therefore, only in less polymerized melts, there are sufficient non-bridging oxygens available to stabilize Y in 6-fold coordination, whereas in highly polymerized melts Y can almost only bond to bridging oxygens. In the latter case, the requirements for local charge balance are achieved by an increase of the mean coordination number of Y and the average Y–O distance. This systematic change of the Y coordination in the quenched melts studied here is very similar to other high field strength elements like Zr^{4+} (Farges et al., 1991) and Th^{4+} (Farges, 1991) data, where $^{[6]}$Zr and $^{[6]}$Th were also found in less polymerized melt compositions, where these cations can bond directly to non-bridging oxygens. For polymerized melt compositions, $^{[8]}$Zr and $^{[8]}$Th were found with longer average bond lengths. For these two cations, the difference in the coordination is even higher than for Y, which is probably related to the higher charge of these cations and thus, the intrinsically higher bond strength.

We would like to stress that although the presented structural data were determined on glasses it is unlikely that they will differ considerably from those in the melt, in accordance to high temperature data on other HFSE. Brown et al. (1995) and Farges et al. (1996b) have shown for HFSE like Zr, Th, Ti and U that no significant change of the coordination during the quench. This is likely due to the high field strength of these cations, which stabilizes the melt configuration during cooling. The strong similarity of the results determined by EXAFS on the CAS-glasses to those obtained by MD provides further evidence that the compositional effect on the local structure of Y is not only present in the glass and is unlikely to differ strongly from that in the melt. To verify this, high temperature EXAFS data are currently being analyzed (Simon et al., 2012b).

5. Conclusion

Our EXAFS analysis of the local structure around Y in the PK-glasses shows that an increase of the $D_{crystal/melt}$ of Y by two orders of magnitude is correlated with an increase of the average bond length by 0.13 Å, and increase of the coordination number from 6 to 8. The differences are mainly attained by a distinct increase in the asymmetry and width of the Y–O pair distribution. The results obtained for the CAS glasses are consistent with those for the PK-glasses and structural parameters obtained by ab-initio simulations (Haigis et al., 2013–this issue). The various local-structure configurations all satisfy local charge requirements. However, in the light of the partition coefficients it can be inferred that the configuration found in less polymerized melts are energetically more favorable than the one found in polymerized melts. Combining molecular dynamics simulations and thermodynamic integration is a possible way to quantify the energy difference for trace elements in different melt compositions as shown for the CAS-melts by Haigis et al. (2013–this issue).

Acknowledgments

We thank HASYLAB at the Deutsches Elektronen-Synchrotron (DESY) for granting beamtime and O. Appelt for help with EMP measurements at GFZ Potsdam. This study was supported by the German Science Foundation (DFG, Wi 2000/6-1) and the French–German DAAD–EGIDE exchange program PROCOPE.

References

Anderson, R., Brennan, T., Mountjoy, G., Newport, R.J., Saunders, G.A., 2000. An EXAFS study of rare-earth phosphate glasses in the vicinity of the metaphosphate composition. Journal of Non-Crystalline Solids (232), 286–292.
Blundy, J.D., Wood, B.J., 1994. Prediction of crystal–melt partition coefficients from elastic moduli. Nature 372 (6505), 452–454.
Brice, J.C., 1975. Some thermodynamic aspects of the growth of strained crystals. Journal of Crystal Growth 28, 249–253.
Brown, I.D., 1981. The Bond–Valence Method: An Empirical Approach to Chemical Structure and Bonding in Crystals. Academic Press, New York.
Brown, I.D., 1996. VALENCE: a program for calculating bond valences. Journal of Applied Crystallography 29, 479–480.
Brown, I.D., Altermatt, D., 1985. Bond–valence parameters obtained from a systematic analysis of the inorganic crystal structure database. Acta Crystallographica. Section B 41, 244–247.
Brown Jr., G.E., Calas, G., Waychunas, G.A., Petiau, J., 1988. X-ray absorption spectroscopy and its applications in mineralogy and geochemistry. Reviews in Mineralogy 18, 431–512.
Brown, G.E. Jr, Farges, F., Calas, G., 1995. X-ray scattering and X-ray spectroscopy studies of silicate melts. Reviews in Mineralogy and Geochemistry 32, 317.
Bunker, G., 1983. Application of the ratio method of EXAFS analysis to disordered systems. Nuclear Instruments and Methods in Physics Research 207, 437–444.

Carroll, M.R., Webster, J.D., 1994. Solubilities of sulfur, noble gases, nitrogen, chlorine, and fluorine in magmas. In: Carroll, M.R., Holloway, J.L. (Eds.), Volatiles in Magmas, vol. 30. Mineralogical Society of America, pp. 231–280.

Daane, A.H., 1968. The Encyclopedia of the Chemical Elements. Reinhold Book Corporation, New York, pp. 810–821.

D'Angelo, P., Di Nola, A., Filipponi, A., Pavel, N.V., Roccatano, D., 1994. An extended X-ray absorption fine structure study of aqueous solutions by employing molecular dynamics simulations. Journal of Chemical Physics 100, 985–994.

Dobrzycki, L., Bulska, E., Pawlak, D.A., Frukacz, Z., Woźniak, K., 2004. Structure of YAG crystals doped/substituted with erbium and ytterbium. Inorganic Chemistry 43 (24), 7656–7664.

Farges, F., 1991. Structural environment around Th^{4+} in silicate glasses: implications for the geochemistry of incompatible Me^{4+} elements. Geochimica et Cosmochimica Acta 55, 3303–3319.

Farges, F., Brown Jr., G.E., 1996. An empirical model for the anharmonic analysis of high-temperature XAFS spectra of oxide compounds with applications to the coordination environment of Ni in NiO, γ-Ni_2SiO_4 and Ni-bearing Na-disilicate glass and melt. Chemical Geology 128 (1), 93–106.

Farges, F., Ponader, C.W., Brown Jr., G.E., 1991. Structural environments of incompatible elements in silicate glass/melt systems: I. Zirconium at trace levels. Geochimica et Cosmochimica Acta 55, 1563–1574.

Farges, F., Brown Jr., G.E., Navrotsky, A., Gan, H., Rehr, J.J., 1996a. Coordination chemistry of Ti (IV) in silicate glasses and melts: II. Glasses at ambient temperature and pressure. Geochimica et Cosmochimica Acta 60 (16), 3039–3053.

Farges, F., Brown Jr., G.E., Navrotsky, A., Gan, H., Rehr, J.J., 1996b. Coordination chemistry of Ti (IV) in silicate glasses and melts: III. Glasses and melts from ambient to high temperatures. Geochimica et Cosmochimica Acta 60 (16), 3055–3065.

Filipponi, A., 2001. EXAFS for liquids. Journal of Physics Condensed Matter 13, 23–60.

Filipponi, A., Di Cicco, A., Natoli, C.R., 1995. X-ray-absorption spectroscopy and n-body distribution functions in condensed matter. I. Theory. Physical Review B, 15122–15134.

Fornasini, P., Monti, F., Sanson, A., 2001. On the cumulant analysis of EXAFS in crystalline solids. Journal of Synchrotron Radiation 8, 1214–1220.

Goldschmidt, V.M., 1937. The principles of distribution of chemical elements in minerals and rocks. Journal of the Chemical Society 655–673.

Green, T.H., 1994. Experimental studies of trace-element partitioning applicable to igneous petrogenesis — Sedona 16 years later. Chemical Geology 117, 1–36.

Haigis, V., Salanne, M., Simon, S., Wilke, M., Jahn, S., 2013. Molecular dynamics simulations of Y in silicate melts and implications for trace element partitioning. Chemical Geology 346, 14–21 (this issue).

Hart, S.R., Davis, K.E., 1978. Nickel partitioning between olivine and silicate melt. Earth and Planetary Science Letters 40, 203–219.

Hazen, R.M., Finger, L.W., 1982. Comparative Crystal Chemistry: Temperature, Pressure, Composition and the Variation of Crystal Structure. John Wiley & Sons, New York.

Irving, A.J., 1978. A review of experimental studies of crystal/liquid trace element partitioning. Geochimica et Cosmochimica Acta 42, 743–770.

Johannsen, A., 1931. A Descriptive Petrography of the Igneous Rocks. University of Chicago Press.

Kevorkov, A.M., Karyagin, V.F., Munchaev, A.I., Uyukin, E.M., Bolotina, N.B., Chernaya, T.S., Bagdasarov, Kh.S., Simonov, V.I., 1995. Y_2O_3 single crystals: growth, structure, and photo-induced effects. Crystallography Reports 40, 23–26.

Kubicki, J.D., Toplis, M.J., 2002. Molecular orbital calculations on aluminosilicate tricluster molecules: implications for the structure of aluminosilicate glasses. American Mineralogist 87, 668–678.

Landron, C., Hennet, L., Coutures, J.P., Jenkins, T., Aletru, C., Greaves, N., Soper, A., Derbyshire, G., 2000. Aerodynamic laser-heated contactless furnace for neutron scattering experiments at elevated temperatures. The Review of Scientific Instruments 71, 1745–1751.

Lytle, F.W., Greegor, R.B., Sandstrom, D.R., 1984. Measurement of soft X-ray absorption spectra with a fluorescent ion chamber detector. Nuclear Instruments and Methods in Physics Research 226, 542–548.

Mountjoy, G., Cole, J.M., Brennan, T., Newport, R.J., Sauders, G.A., Wallidge, G.W., 2001. A rare earth L_3-edge EXAFS and L_1-edge XANES study of Ce, Nd and Eu phosphate glasses and crystals in the composition range from metaphosphate to ultraphosphate. Journal of Non-Crystalline Solids 279, 20–27.

Mustre de Leon, J., Rehr, J.J., Zabinsky, S.I., Albers, R.C., 1991. Ab initio curved-wave X-ray-absorption fine structure. Physical Review B 44, 4146–4156.

Mysen, B.O., 1990. Relationships between silicate melt structure and petrologic processes. Earth-Science Reviews 27, 281–365.

Mysen, B.O., Richet, P., 2005. Silicate Glasses and Melts, Properties and Structure. Elsevier, Amsterdam.

Mysen, B.O., Virgo, D., Seifert, F.A., 1985. Relationships between properties and structure of aluminosilicate melts. American Mineralogist 70, 88–105.

Neuville, D., Cormier, L., Massiot, D., 2006. Al coordination and speciation in calcium aluminosilicate glasses: effects of composition determined by ^{27}Al MQ-MAS NMR and Raman spectroscopy. Chemical Geology 229 (1), 173–185.

Newville, M., 2001. IFEFFIT: interactive XAFS analysis and FEFF fitting. Journal of Synchrotron Radiation 8, 322–324.

Onuma, N., Higuchi, H., Wakita, H., Nagasawa, H., 1968. Trace element partition between two pyroxenes and the host lava. Earth and Planetary Science Letters 5, 47–51.

Park, B., Li, H., Corrales, L.R., 2002. Molecular dynamics simulation of La_2O_3–Na_2O–SiO_2 glasses. I. The structural role of La^{3+} cations. Journal of Non-Crystalline Solids 297, 220–238.

Pauling, L., 1929. The principles determining the structure of complex ionic crystals. Contribution from Gates Chemical Laboratory, California Institute of Technology, 51, pp. 1010–1026.

Peters, P.M., Houde-Walter, S.N., 1997. X-ray absorption fine structure determination of the local environment of Er^{3+} in glass. Applied Physics Letters 70, 541–543.

Poe, B.T., McMillan, P.F., Angell, C.A., Sato, R.K., 1992. Al and Si coordination in SiO_2–Al_2O_3 glasses and liquids: a study by NMR and IR spectroscopy and MD simulations. Chemical Geology 96, 333–349.

Ponader, C.W., Brown, G.E. Jr, 1989. Rare earth elements in silicate systems: I. Effects of composition on the coordination environments of La, Gd, and Yb. Geochimica et Cosmochimica Acta 53, 2893–2903.

Price, S.W.T., Zonias, N., Skylaris, C.-K., Hyde, T.I., Ravel, B., Russell, A.E., 2012. Fitting EXAFS data using molecular dynamics outputs and a histogram approach. Physical Review B 85, 075439.

Prowatke, S., Klemme, S., 2005. Effect of melt composition on the partitioning of trace elements between titanite and silicate melt. Geochimica et Cosmochimica Acta 69 (3), 695–709.

Ravel, B., Newville, M., 2005. ATHENA, ARTEMIS, HEPHAESTUS: data analysis for X-ray absorption spectroscopy using IFEFFIT. Journal of Synchrotron Radiation 12, 537–541.

Ribar, B., Milinski, N., Budovalcev, Z., Krstanovic, I., 1980. Tetraaquatri(nitrate yttrium(III)) dihydrate, Y $(H_2O)_4$ $(NO_3)_3 \cdot 2$ H_2O. Acta Crystallographica Section C: Crystal Structure Communications 9, 203–206.

Rickers, K., Drube, W., Schulte-Schrepping, H., Welter, E., Brüggmann, U., Hermann, M., Heuer, J., Schulz-Ritter, H., 2007. New XAFS Facility for In-Situ Measurements at Beamline C at HASYLAB. AIP Conf. Proc., 882, pp. 905–907.

Risbud, S.H., Kirkpatrick, R.J., Taglialavore, A.P., Montez, B., 1987. Solid-state NMR evidence of 4-, 5-, and 6-fold aluminum sites in roller-quenched SiO_2-$A1_2O_3$ glasses. Journal of the American Ceramic Society 70 (1), 10–12.

Rossano, S., Ramos, A., Delaye, J.-M., Crux, S., Filipino, A., Brouder, Ch., Calas, G., 2000. EXAFS and molecular dynamics combined study of CaO–FeO–$2SiO_2$ glass. New insight into site significance in silicate glasses. Europhysics Letters 49, 597–602.

Ryerson, F.J., Hess, P.C., 1978. Implications of liquid–liquid distribution coefficients to mineral–liquid partitioning. Geochimica et Cosmochimica Acta 42, 921–932.

Schmidt, M.W., Connolly, J.A.D., Günther, D., Bogaerts, M., 2006. Element partitioning: the role of melt structure and composition. Science 312, 1646–1650.

Sen, S., 2000. Atomic environment of high-field strength Nd and Al cations as dopants and major components in silicate glasses: a Nd LIII-edge and Al K-edge X-ray absorption spectroscopic study. Journal of Non-Crystalline Solids 261, 226–236.

Sen, S., Stebbins, J.F., 1995. Structural role of Nd^{3+} and Al^{3+} cations in SiO_2 glass: a 29Si MAS-NMR spin–lattice relaxation, ^{27}Al NMR and EPR study. Journal of Non-Crystalline Solids 188, 54–62.

Sevillano, E., Meuth, H., Rehr, J.J., 1979. Extended X-ray absorption fine structure Debye–Waller factors. I. Monatomic crystals. Physical Review B 20, 4908–4911.

Shannon, R.D., 1976. Revised effective ionic radii and systematic studies of interatomic distances in halides and chalcogenides. Acta Crystallographica 32, 751–767.

Simon, S., Wilke, M., Klemme, S., Caliebe, W.A., Chernikov, R., Kvashnina, K., 2012a. The Influence of the Composition on the Local and Electronic Structure of Trace Elements in Quenched Melts. 14th International Conference on Experimental Mineralogy Petrology Geochemistry, Kiel.

Simon, S., Wilke, M., Klemme, S., Chernikov, R., 2012b. The Influence of Melt Composition on the Local Structure around Trace Elements in Glasses and Melts with Implications for Crystal–Melt Partitioning. 481, European Mineralogical Conference, Frankfurt.

Stebbins, J.F., Oglesby, J.V., Kroeker, S., 2001. Oxygen triclusters in crystalline $CaAl_4O_7$ (grossite) and in calcium aluminosilicate glasses: ^{17}O NMR. American Mineralogist 86, 1307–1311.

Stern, E.A., 1974. Theory of the extended X-ray-absorption fine structure. Physical Review B 10, 3027–3037.

Stern, E.A., Livnš, P., Zhang, Z., 1991. Thermal vibration and melting from a local perspective. Physical Review B 43, 8850–8860.

Teo, B., 1986. EXAFS: Basic Principles and Data Analysis. Springer, Berlin.

Toplis, M.J., Corgne, A., 2002. An experimental study of element partitioning between magnetite, clinopyroxene and iron-bearing silicate liquids with particular emphasis on vanadium. Contributions to Mineralogy and Petrology 144, 22–37.

Tröger, L., Arvanitis, D., Baberschke, K., Michaelis, H., Grimm, U., Zschech, E., 1992. Full correction of the self-absorption in soft-fluorescence extended X-ray-absorption fine structure. Physical Review B 46, 3283–3289.

van Westrenen, W., Blundy, J.D., Wood, B.J., 2001. High field strength element/rare earth element fractionation during partial melting in the presence of garnet: Implications for identification of mantle heterogeneities. Geochemistry, Geophysics, Geosystems 2 (2000GC000133).

Watson, E.B., 1976. Two-liquid partition coefficients: experimental data and geochemical implications. Contributions to Mineralogy and Petrology 56 (1), 119–134.

Wilding, M., Badyal, Y., Navrotsky, A., 2007. The local environment of trivalent lanthanide ions in sodium silicate glasses: a neutron diffraction study using isotopic substitution. Journal of Non-Crystalline Solids 353 (52), 4792–4800.

Wood, B.J., Blundy, J.D., 1997. A predictive model for rare earth element partitioning between clinopyroxene and anhydrous silicate melt. Contributions to Mineralogy and Petrology 129, 166–181.

Wood, B.J., Blundy, J.D., 2001. The effect of cation charge on crystal–melt partitioning of trace elements. Earth and Planetary Science Letters 188, 59–71.

Yevick, A., Frenkel, A.I., 2010. Effects of surface disorder on EXAFS modeling of metallic clusters. Physical Review B 81, 115451.

Zabinsky, S.I., Rehr, J.J., Ankudinov, A., Albers, R.C., Eller, M.J., 1995. Multiple-scattering calculations of X-ray-absorption spectra. Physical Review B 52, 2995–3009.

Zen, E.-A.N., 1986. Aluminum enrichment in silicate melts by fractional crystallization: some mineralogic and petrographic constraints. Journal of Petrology 27, 1095–1117.